Free-Flight Aerodynamics of Ellipsoidal Clusters in Hypersonic Flow

R. Chase Latyak[1] and Stuart J. Laurence[2]
University of Maryland, College Park, MD, 20742, United States

Characterizing the separation behavior of meteoroids in the atmosphere is critical in risk assessment and mitigation. This work aims to better understand the separation behavior of meteoroid fragments by examining clusters of small spheres, arranged in initial ellipsoidal clusters of varying eccentricity. Hypersonic free-flight experiments were conducted at Mach 6 to study and quantify the separation behavior of these ellipsoidal clusters. Each experiment contained 52 equal sized plastic spheres packed within a 3D printed shell that would separate in a nondisruptive manner upon flow arrival. A machine learning algorithm was employed to initially identify and categorize spheres. Then, lone spheres were tracked using subpixel edge detection routines, whereas occluded spheres or sub-clusters were tracked with artificial image generation techniques. Streamwise and lateral sphere velocities were calculated by tracking each sphere position over subsequent frames, to quantify the late separation behavior. Comparisons are drawn between clusters of differing initial shapes, as well as prior data on perfectly spherical clusters, and a trend in collective lateral velocity is established.

I. Introduction

Meteoroids frequently enter the Earth's atmosphere, and although a substantial percentage of those meteoroids burn up in the atmosphere before impact, the chance of surface impact poses significant threats to people and property [1]. Smaller bodies on the order of 10-100 meters that cannot be easily tracked pose the highest risk to humans [2]. The front surfaces of these smaller meteoroids experience extremely high pressures, typically of the order of $\rho_a V^2$, where ρ_a is the density of the atmosphere and V is the speed of the meteoroid, relative to the atmosphere. This extreme pressure ultimately leads to fragmentation [2]. The lateral velocities of the fragments, caused by aerodynamic interactions with the atmosphere, can significantly increase both atmospheric energy deposition and ground damage.

Attempting to better understand and characterize the separation behavior of meteoroids, particularly the lateral velocities of fragments, is critical to effectively predict and model how these objects break apart and where on the surface impact risk is highest. As such, performing free-flight experiments in hypersonic flow conditions is one way in which researchers have learned more about the separation behavior of clusters of bodies. Previous studies [3-5] have been conducted on spherical clusters, composed of equal sized spheres, unequal spheres, and mixtures including dust. The results of these studies proposed a power law relation between collective lateral velocity and cluster population and validated this power law relation for clusters of higher population, up to the order of 1,000. The present work aims to build upon these previous studies to better understand the separation behavior of meteoroid fragments by examining ellipsoidal clusters of small, equally sized spheres and investigating how initial cluster shape impacts overall separation behavior. Specifically, the quantity of primary interest is the collective lateral velocity of each cluster shape, and if there is a clear trend between cluster shape and this collective lateral velocity.

It is also important to review the governing assumptions that are being made for these experiments, and how they are supported in the context of real-world meteoroid fragmentation. First, it is assumed that the fragments themselves are all perfectly spherical. This assumption is common in meteoroid fragmentation studies [6, 7], but true meteoroid fragments are often nonspherical, so the present assumption should be taken as a lower limit on fragment dispersal [8, 9]. Second, it is assumed that fragments are released instantaneously and with no initial velocity. Realistic sources of initial fragment velocity include release of strain energy and parent body rotation, but Laurence & Deitering [10] have shown that these initial velocities are generally negligible compared to velocities achieved through aerodynamic

[1] Undergraduate Student, Department of Aerospace Engineering, AIAA University Student Member 1924682.
[2] Associate Professor, Department of Aerospace Engineering, AIAA Associate Fellow.

effects. Third, the Mach 6, perfect flow conditions assumed in hypersonic wind tunnel tests in this work are representative of conditions typically experienced by meteoroids in a fragmentation event. Although Mach 6 is well below that of expected values for meteoroid entry, the Mach number independence principle [11] states that flow field characteristics and aerodynamic coefficients hold nearly constant above a certain Mach number, given inviscid, perfect-gas conditions. For the blunt, spherical bodies in this work, properties freeze above roughly Mach 5, indicating that the assumption made about flow conditions is valid even for higher Mach numbers observed in actual meteoroid entry.

With some motivations, background information, and assumptions now stated, the remainder of this work is structured as follows. Section II details the experimental setup utilized in this research, including both the physical laboratory setup and the image processing and analysis techniques employed to extract useful data from the experiments. Section III discusses the main results and data, presenting both qualitative and quantitative analysis of cluster separation behavior. Section IV provides a review and conclusion of the work, as well as proposing potential next steps in the field.

II. Experimental Setup

A. Facility

Hypersonic free-flight experiments were performed in the HyperTERP Mach 6 reflected shock tunnel in the High-Speed Aerodynamics and Propulsion Laboratory at the University of Maryland, College Park. This tunnel is 15m long, with a full schematic, adapted from [3], shown in Fig. 1. A double diaphragm separates the driver section from the driven section, and a single diaphragm separates the driven section from the nozzle, test section, and dump tank. The driven and driver sections are pressurized with a mixture of air and helium. To fire the tunnel, the space between the double diaphragm is opened to vacuum, due to a small secondary vacuum pump, and thus the pressure difference between the driver and this space causes the diaphragms to burst sequentially.

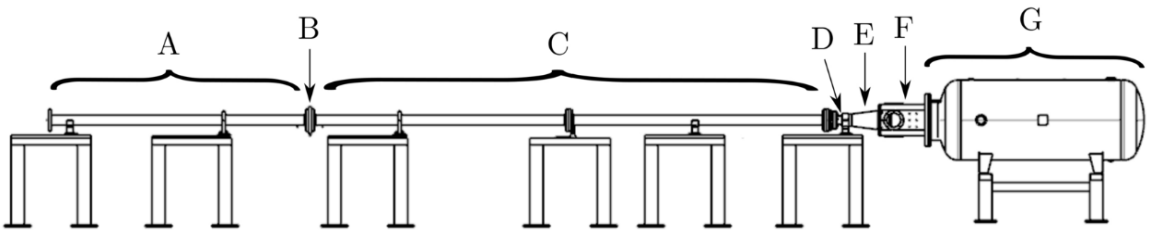

Fig. 1 HyperTERP Schematic: A is the driver section, B is the double diaphragm, C is the driven section, D is the secondary, single diaphragm, E is the Mach 6 nozzle, F is the test section, and G is the dump tank.

The tunnel can operate over a range of conditions, with stagnation pressures of up to 2 MPa and temperatures up to 1600 K. For all the runs conducted in this work, freestream conditions were kept the same, with a driven pressure of 56.3 kPa, driver pressure of 2.05 MPa, and a temperature of 300 K. The steady test time can vary based on initial tunnel conditions, but for these experiments the steady test time lasted around 12-13 milliseconds.

B. Model Suspension and Test Configurations

The models, referred to in this work as "shells," are adapted from Whalen's design [3, 5] that has been utilized successfully in previous HyperTERP experiments. The main structure of the shell is 3D printed using a stereolithography (SLA) printer with a photopolymer resin. To create shells that would result in ellipsoidal initial clusters, the computer-aided design (CAD) model for the spherical shell was either stretched or compressed according to the desired eccentricity. The stretched models were then scaled to ensure that the internal cavity volume of 1767 mm^3 (inner shell diameter of 15 mm) was the same among all conditions. This volume was calculated based on the total volume occupied by 52 spheres with a diameter of 3.175 mm, which is roughly 871 mm^3. A chosen loading factor of 0.5 yielded a required volume of 1743 mm^3. Real-world testing validated that this volume allowed exactly 52 spheres to fit comfortably inside, without requiring any force to pack spheres in, to mitigate unwanted disturbances upon shell release. The main goal of the shell mechanism is to separate cleanly without interfering with any of the spheres contained inside, achieved through the aerodynamic design of both the front and rear flaps. A diagram of the shell can be seen below in Fig. 2, with the key features labeled in the caption.

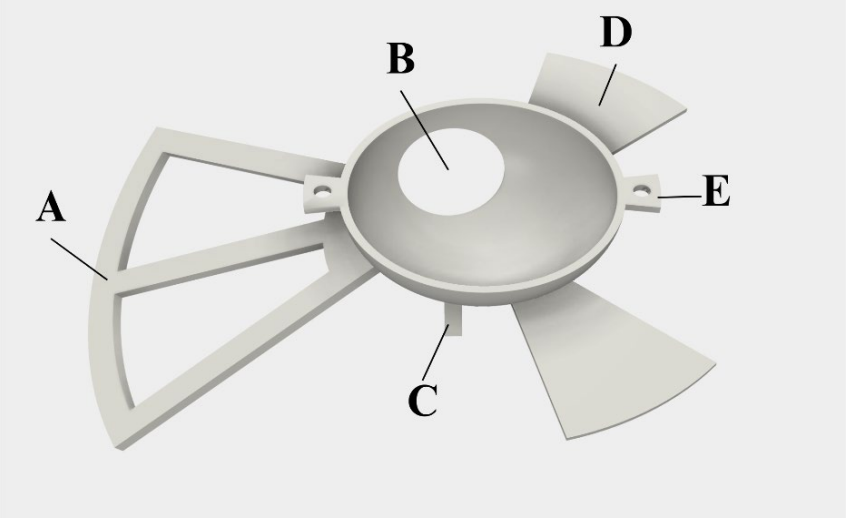

Fig. 2 CAD model of shell with key features: A is the forward flap, B is the hole to load spheres, C is the anchor point, D is a rear flap, and E is a dowel hole.

The test matrix for this work contained four unique ellipsoidal cluster conditions, each repeated twice. All conditions used 52 equally sized 1/8" (3.175 mm) diameter spheres made from polytetrafluoroethylene (PTFE), which has a density of 2130 kg/m^3. Some initial experiments and previous works utilized Delrin acetal plastic (ρ = 1400 ± 40 kg/m^3) [5]. However, the denser PTFE spheres allowed for better visualization of initial cluster shape and separation, as the shells were further expelled before significant sphere movement occurred. In this work, four different shell shapes were tested to quantify the separation behavior for clusters of different initial shapes. Instead of referring to eccentricity, each shell shape condition is referred to in terms of the streamwise length factor, specifically being 1.5x, 1.25x, 0.75x, and 0.5x, where a perfectly spherical cluster would simply be 1x. The experiments in this work were all set up to be at 0° angle of attack, so that the forward flaps face the oncoming flow. Fig. 3 showcases the four conditions tested, each at rest before flow arrival.

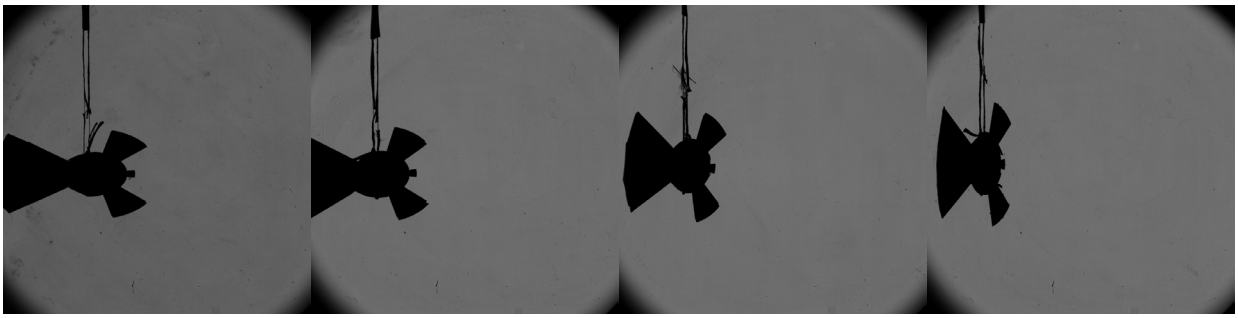

a) b) c) d)

Fig. 3 a) 1.5x condition, b) 1.25x condition, c) 0.75x condition, and d) 0.5x condition.

The setup of the model itself first required manual removal of the supports from the 3D printing process. The remnants of the supports were smoothed out where needed, and the inner surface of the shell itself, where the spheres were located, did not contain any supports to minimize surface roughness that could affect the sphere separation. The hollowed front flaps were covered with Kapton tape to provide the necessary surface area to pull the shell apart while maintaining a center of mass that was far enough back to hang at 0° angle of attack. To suspend the spheres, dental floss was tied to both anchor points. The two pieces of floss were connected with clear adhesive tape, so that the length of the floss below the tape resulted in 0° roll. Above this piece of tape, both pieces of floss were heavily frayed to ensure that they would break instantly upon flow arrival. To mount the model to the test section, the floss was secured around two metal rings screwed into the top of the test section, and the remaining length of floss was stuck to the outside of the tunnel with putty. The combination of the clear tape, rings, and angle of attaching the loose end of the floss made it possible to suspend the model at 0° roll, yaw, and angle of attack as desired. In most cases, small strips of painter's tape were used to keep the two halves of the shell from separating prematurely, either while hanging the

shell or pulling the test section to vacuum. The painter's tape was chosen as it was sticky enough to keep the two shell halves together, but not too sticky to keep them together or interfere when the flow reached the test section. The following photo, Fig. 4, shows an example of a shell that is suspended in the test section of HyperTERP with the aforementioned techniques.

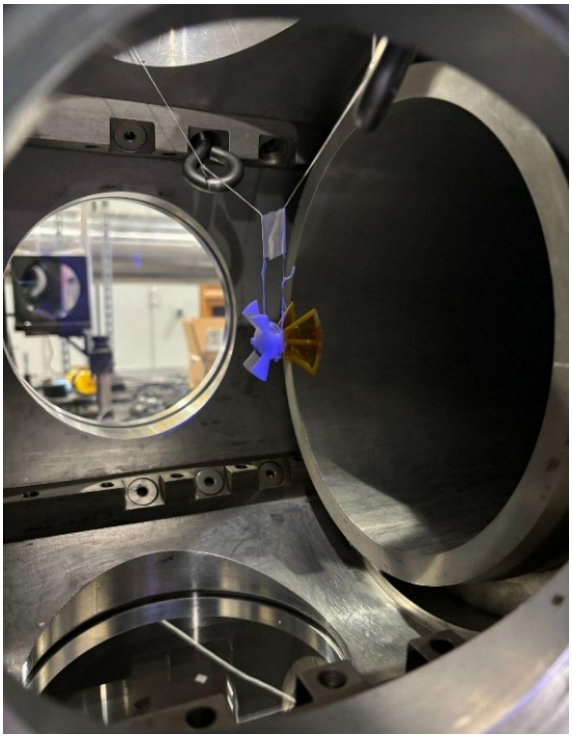

Fig. 4 Photo of an ellipsoidal shell containing spherical fragments suspended in the test section of HyperTERP.

C. Visualization and Tracking Techniques

High-speed cameras captured images from two, approximately orthogonal, optical axes. The horizontal axis employed a Z-type Schlieren system that used an LED light source and collimation through spherical mirrors to provide clear, focused, well-lit images. Since the light passing through the test section of the wind tunnel was collimated, line of sight displacements of the spheres did not correspond to any apparent changes in the images, so all the spheres in the image looked identical regardless of their relative location in space. To visualize the spanwise distribution of the spheres, the vertical optical axis was used. In contrast, the vertical axis employed a simple backlit visualization with a narrow depth of field. To improve focusing on spheres that were closer to or further away from the camera than the focusing plane, the aperture of the camera was significantly closed which resulted in darker images. Image brightness was thus increased in post-processing before spheres were identified to enhance the edge contrast of the spheres.

Sphere detection was achieved using a machine learning (ML) algorithm. Once the ML program detected all the spheres in an image, the spheres were categorized into lone spheres and those that were partially occluded by surrounding spheres. Lone spheres were tracked using a subpixel edge detection routine [12], whereas occluded spheres were tracked using an artificial image generation routine [13]. The reliability of identifications for highly occluded groups of spheres was lower than that of individual spheres, but the data of interest were primarily velocities in the late separation stages. As the clusters separated, there were few instances of highly occluded spheres where these techniques would fail to locate properly, seen in the following images. Images a) and b) in Fig. 5 showcase accurate identification of every sphere in the frame, whereas image c) indicates how these techniques can occasionally struggle for highly occluded groups of spheres.

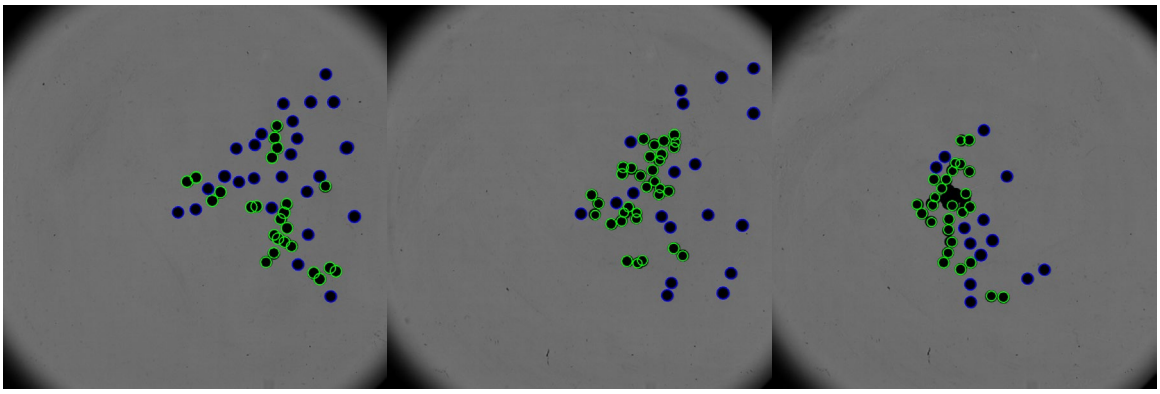

a) b) c)

Fig. 5 Examples of separation images: blue circles represent isolated spheres located with edge detection, whereas green circles represent occluded spheres located with artificial image generation.

To ensure the most accurate results possible, a few preliminary measures were taken to adjust the datasets. In cases like image c) in Fig. 5 where there are clearly spheres that were not identified, the estimated centroid and radius were manually added to the dataset. The same solution was applied in cases where the spheres were not identified due to low edge contrast on out-of-focus spheres from the bottom perspective. The manual addition of data points ensured that every sphere visible in the image had a corresponding velocity value that was calculated.

III. Results

A. Definitions and Formulas

In order to present the results of the experiments performed, some important quantities and formulas must first be defined. Moving forward, the results will be discussed primarily in terms of the *x*, *y*, and *z* axes, which are defined as follows: *x* is the streamwise direction, *y* is the vertical, or transverse, direction (optical axis for the bottom view), and *z* is the horizontal, or spanwise, direction (optical axis for the side view). This means that the side view provides information on the *x* and *y* velocities and the bottom view provides information on the *x* and *z* velocities. By combining the data obtained from these two orthogonal axes, the full state and velocity vector, as well as lateral velocity, can be determined.

Velocities represented with a prime symbol indicate a normalized quantity, which is done to provide insightful results beyond the specific flow conditions of the tunnel for these experiments. First, a common nondimensionalization is employed, with the velocity scale [5]:

$$V_s = \sqrt{\frac{\rho_\infty}{\rho_{sph}}} u_\infty \,, \tag{1}$$

where ρ_∞ is the freestream density, ρ_{sph} is the sphere density, and u_∞ is the freestream velocity. The transverse velocities for all spheres are calculated based on the nonstationary cluster center of mass. Thus, the individual relative position and individual transverse velocity are defined respectively:

$$\vec{x}_{rel,i} = (\vec{x}_i - \vec{x}_{com}) - (\vec{x}_i - \vec{x}_{com})_{\hat{x}} \,, \tag{2}$$

$$V_{T,i} = \left(\vec{V}_i - \vec{V}_{com}\right) \cdot \frac{\vec{x}_{rel,i}}{\|\vec{x}_{rel,i}\|} \,. \tag{3}$$

In Eqs. (2, 3), the "com" subscript denotes a quantity for the cluster center of mass, "rel" denotes relative to the center of mass, and "i" represents the quantity for an individual sphere. Note that the relative position does not consider the streamwise component, or in other words, the lateral velocity is purely in the *y*-*z* plane. To quantify the behavior of the entire cluster, another quantity called the collective lateral velocity is defined by:

$$\bar{V}_T = \frac{1}{N} \sum V_{T,i} \,, \tag{4}$$

where N is the total number of spheres in the cluster. Both the individual lateral velocities and the collective lateral velocity can then be nondimensionalized as seen in Eqs. (5, 6). The term "collective lateral velocity" used in later sections refers to the nondimensional value in Eq. (6) as opposed to the dimensional quantity in Eq. (4).

$$V'_{T,i} = V_{T,i}/V_s \,, \tag{5}$$

$$\bar{V}'_T = \bar{V}_T/V_s \,. \tag{6}$$

B. Individual Sphere Velocity Calculation

The first step in analyzing and quantifying the results of these experiments was calculating the individual sphere velocities. Videos capture the entire separation process, from initial flow arrival to late-stage separation, as seen from left to right in Fig. 6. The focus when determining sphere velocities was primarily in the late-stage separation region.

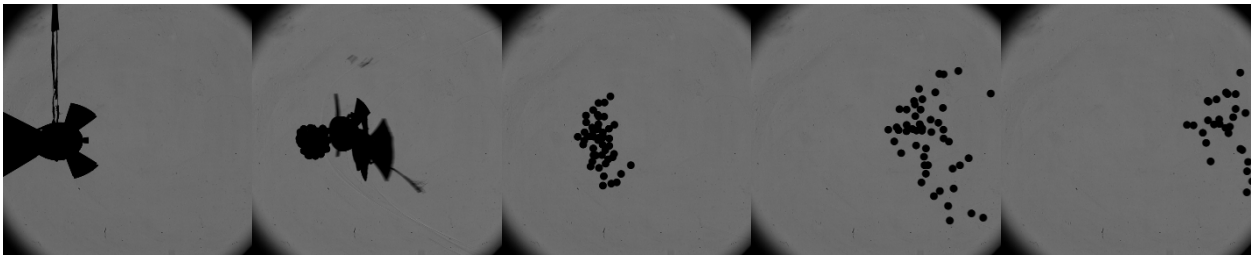

Fig. 6 Schlieren image sequence of typical cluster separation behavior.

Streamwise and lateral sphere velocities were calculated by tracking each sphere position over subsequent frames, to quantify the late separation behavior. To fairly compare clusters of varying starting points, velocities were analyzed at a set cutoff point, which was 600 pixels past the original centroid of the shell when suspended. A linear polyfit based on up to eight previous centroid positions gave a velocity for each sphere in the experiment. To ensure accurate results and eliminate errors based on misclassified spheres or continuity breaks in sphere identification, several adjustments were implemented. Identification results with a radius outside of reasonable bounds were overwritten to become an empty set. Additionally, it was possible, especially in occluded groups, for one sphere to be identified twice by the machine learning algorithm. For each image, all sphere data were examined automatically and if a matching or extremely close pair of centroid coordinates was found, the data point with a radius further from the average sphere radius was deleted. Lastly, since velocities were calculated with a linear fit, if there were fewer than four points found for a specific sphere, that velocity was discarded to avoid inaccuracies from small samples of data or a small positional error in one frame of the sequence. That velocity was then attempted to be calculated in a later frame, close to the standard cutoff, if there were enough subsequent frames for an accurate result. Images were generated, such as those seen in Fig. 7, to visualize and ensure accurate results for each sphere in the cluster.

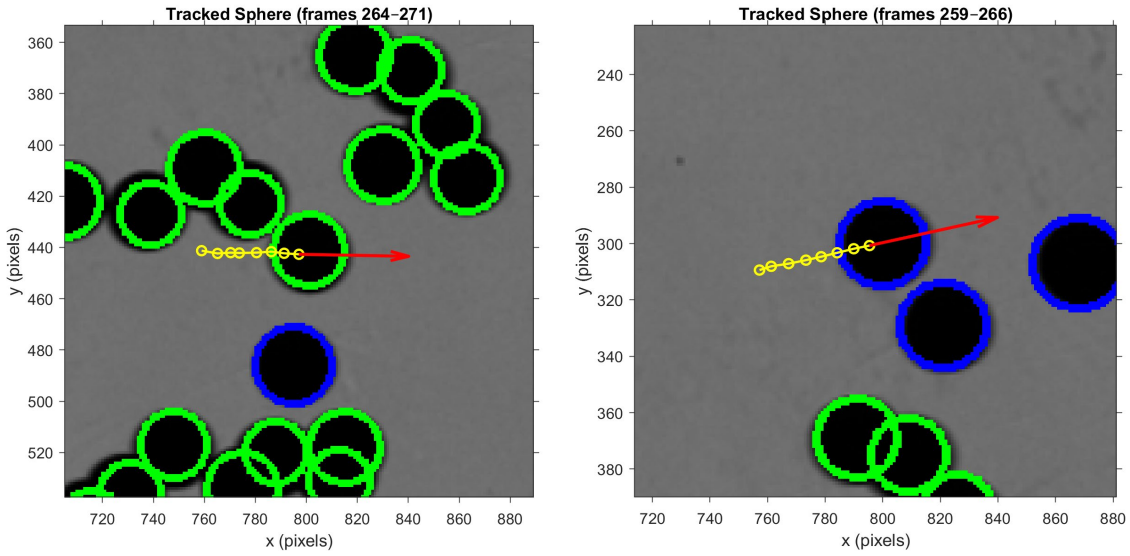

a) b)

Fig. 7 Examples of sphere velocity results, where yellow dots represent the centroid of a sphere over subsequent frames, and the red arrow is the calculated velocity of that sphere.

The combination of automated error correction with manual data adjustment ensured reasonable results for each sphere in each test condition. It should be noted that in some cases, less than 52 velocities were calculated for purposes of determining the collective lateral velocity, and there are two main causes for this discrepancy. First, some experiments, particularly those involving the 0.5x condition, had spheres that were perturbed by the shell itself and thus were either not visible or did not provide useful information regarding true free-flight separation behavior. Alternatively, some clusters of occluded spheres remained too occluded to sufficiently pick out distinct spheres from either viewing axis, making it appear as if there are fewer spheres than truly present. All experiments contained between 50 and 52 spheres that could be accurately quantified, which was enough to produce a meaningful result in terms of collective lateral velocities. The repeated conditions also helped to provide more insight and reduce the possibility of one anomalous result heavily skewing the final collective lateral velocity.

C. Collective Lateral Velocity Calculation

Collective lateral velocities were calculated for each of the eight tests, using Eqs. (1-6) as described previously to calculate a relative velocity scale, position and velocity relative to the cluster center of mass, and the nondimensionalized collective lateral velocity. Table 1 contains the results of the collective lateral velocity calculations for each test condition, with the two values in the right column representing two separate runs at each condition.

Table 1 Collective Lateral Velocity by Condition.

Test Condition	$\bar{V}_T'$
1.5x	0.8600, 0.8463
1.25x	0.9158, 0.8453
0.75x	0.7740, 0.6292
0.5x	0.7573, 0.6043

Although the values between repetitions of a certain condition did not always align, as may be expected due to variability and randomness that occurs in sphere separation experiments, there was an evident trend between the collective lateral velocity and the eccentricity and orientation of the clusters. As the streamwise length factor of the ellipsoidal clusters decreased, so too did the overall lateral velocities that were observed. In particular, there was a noticeable difference between the lateral velocities observed in the 1.5x and 1.25x cases compared to those seen in the 0.75x and 0.5x clusters. However, the values for the 1.5x and 1.25x conditions were comparable with each other, as were the values for the 0.75x and 0.5x configurations. In addition, the values at the 1.5x and 1.25x were higher than the typical collective lateral velocity observed in spherical clusters [3], whereas the 0.75x and 0.5x conditions were generally lower than the spherical case, further reinforcing this observed trend. The values for spherical collective velocities were also obtained in the same experimental conditions with the same number of spheres, 52. These trends and comparisons between collective lateral velocities and cluster shape can be seen graphically in Fig. 8.

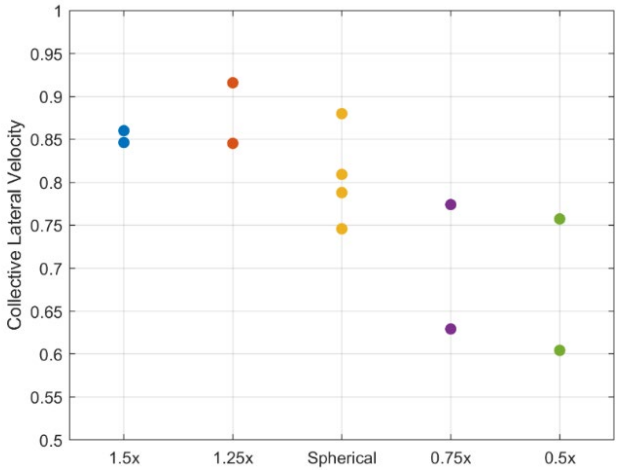

Fig. 8 Collective lateral velocity values plotted against initial cluster shape.

This trend could be explained, at least in part, by the orientation of the semi-major axis of the ellipsoidal clusters. For the 1.5x and 1.25x conditions, the semi-major axis was aligned with the flow direction, but the 0.75x and 0.5x conditions had a semi-major axis aligned in the y direction, as defined previously. Qualitatively, typical free-flight cluster experiments observe a flattening, or pancaking, phenomenon in the early portion of separation, which means that the cluster tends to compress in the x direction. For the 0.75x and 0.5x cases, part of this flattening was already achieved by the ellipsoidal cluster configuration, so these clusters experienced less flattening and less radial expansion, meaning that the ultimate lateral velocity values were lower. On the contrary, the conditions that were longer in the x direction experienced more intense flattening in the early phase of separation and thus more spheres were forced outwards, resulting in higher lateral velocities. So, there were slight differences observed between each condition, but the major factor that determined collective lateral velocity was the orientation of the ellipsoid relative to the oncoming flow, as opposed to just the eccentricity.

In addition to the collective lateral velocity values, the individual sphere velocities provided useful information on the overall separation behavior. Since the calculation of a collective lateral velocity inherently required knowledge of each sphere's x, y, and z velocities, these components can be represented individually on a scatterplot. In particular, the nondimensionalized y and z velocities relative to the velocity of the cluster center of mass can be calculated as follows:

$$V'_{y,i} = V_{y,rel,i}/V_s \,, \tag{7}$$

$$V'_{z,i} = V_{z,rel,i}/V_s \,. \tag{8}$$

The results from each experiment were plotted in Figs. 9-12, with the collective lateral velocity of the associated experiment overlaid as a black dashed circle on the plot. Since each ellipsoidal condition was tested twice, the two repetitions are plotted separately next to each other. Each individual point on the scatterplot represents the unique y and z normalized velocity for a particular sphere, as calculated from Eqs. (7, 8).

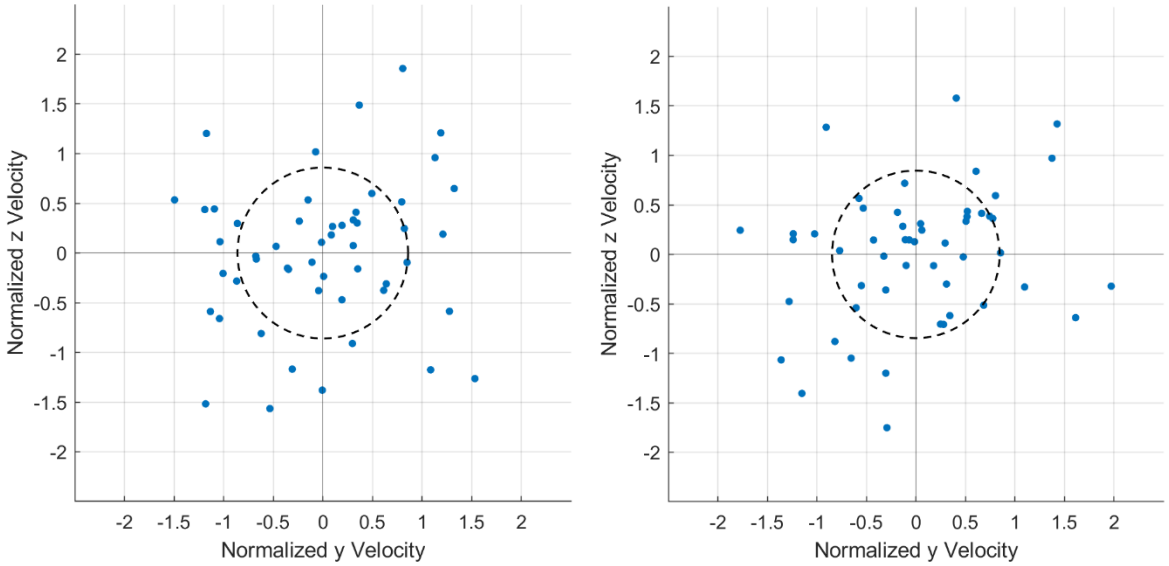

a) b)

Fig. 9 1.5x condition: normalized y velocity vs. normalized z velocity scatterplot with collective lateral velocity shown by the dashed black line.

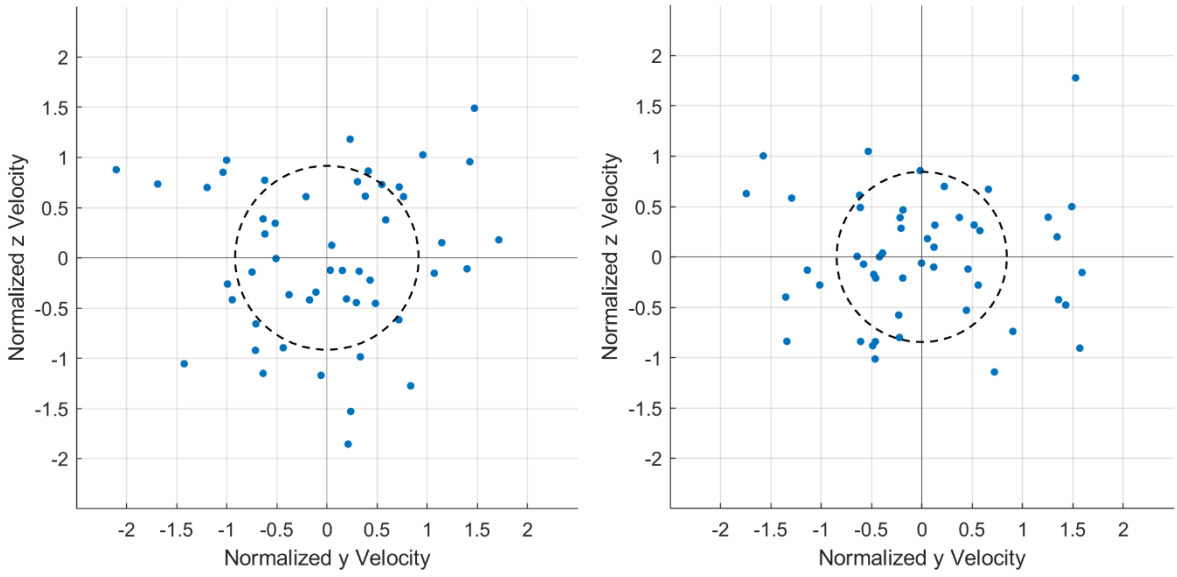

a) b)

Fig. 10 1.25x condition: normalized *y* velocity vs. normalized *z* velocity scatterplot with collective lateral velocity shown by the dashed black line.

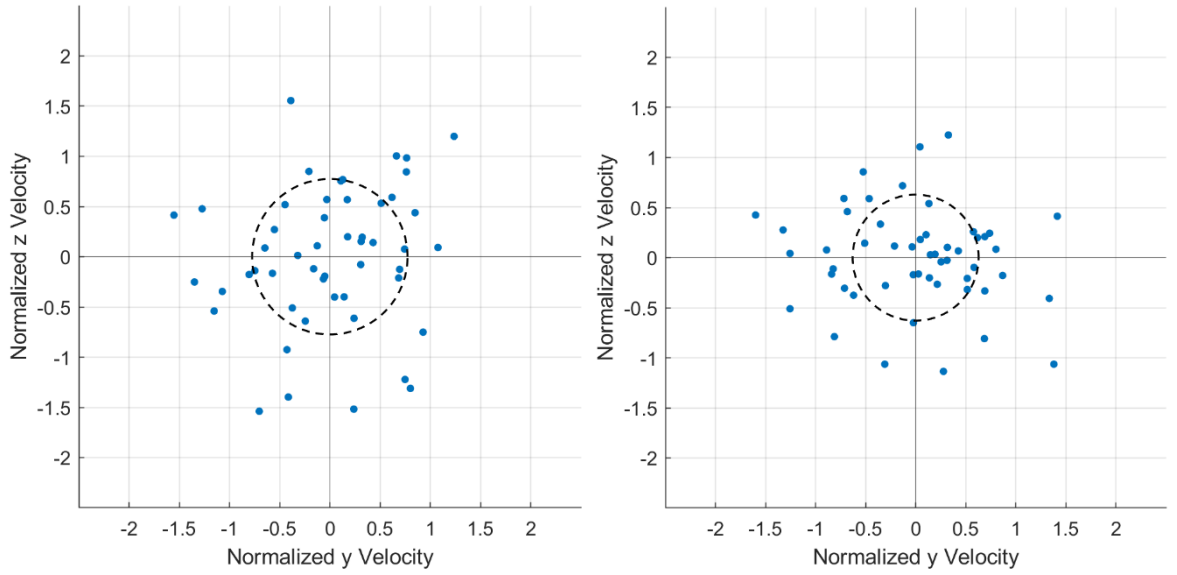

a) b)

Fig. 11 0.75x condition: normalized *y* velocity vs. normalized *z* velocity scatterplot with collective lateral velocity shown by the dashed black line.

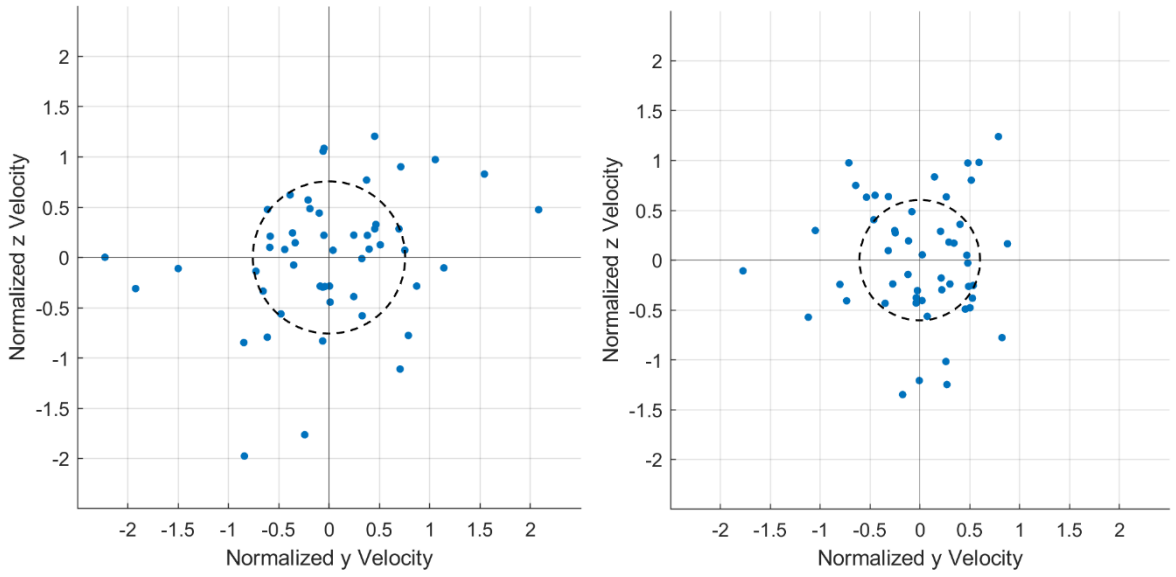

a) b)

Fig. 12 0.5x condition: normalized *y* velocity vs. normalized *z* velocity scatterplot with collective lateral velocity shown by the dashed black line.

One of the major results determined from previous experiments by Laurence, Whalen, and Zhu [3-5] was the correlation between collective lateral velocity and number of discrete fragments in a cluster. Results showed that number of bodies had a significant effect on this collective lateral velocity value, ranging from <0.3 for just 2-4 spheres [3] all the way to >2 for 1,000 spheres [4]. The power law fit that was determined is given by:

$$\bar{V}_T' = 0.123(N-2)^{0.407} + \bar{V}_{T,N=2}' \,, \tag{9}$$

where $\bar{V}_{T,N=2}' = 0.22$. Comparing the results of this study back to the power law fit, it can be expected for ellipsoidal clusters extended in the flow direction to exhibit a collective lateral velocity slightly higher than that predicted by the power law fit, since Eq. (9) was derived from the results of spherical cluster separation only. On the contrary, ellipsoidal clusters that are compressed in the streamwise direction, or in other words have a semi-major axis orthogonal to the streamwise direction, would be expected to have collective lateral velocities lower than the power fit law for a given number of spheres in the cluster.

IV. Conclusions and Future Work

To better quantify the separation behavior of nonspherical clusters representative of meteoroid fragmentation, an experimental campaign consisting of hypersonic free-flight experiments was conducted. An ellipsoidal shell mechanism was employed to noninvasively release the cluster upon flow arrival. The configurations of clusters were either extended or compressed in the streamwise direction by a factor of 1.5, 1.25, 0.75, or 0.5, and were tested to observe trends between cluster shape and separation behavior. Optical tracking techniques and novel machine learning identification algorithms were utilized to obtain results for both individual and collective lateral velocities of fragments. The results indicated a relationship, where more compressed clusters, or those that were shorter in the streamwise direction, resulted in lower lateral velocities, and vice versa for the extended configurations.

The results of this study shed light on the differences between spherical and ellipsoidal meteoroid fragmentation, supported by experimental data, but there is still future work to be done in the field to better understand and fully characterize these phenomena. First, configurations with only mild eccentricities were tested, due to both 3D printing limitations as well as the ability to release the cluster without disturbing spheres using the present shell mechanism. Future studies should seek to further explore more extreme cluster shapes, perhaps including more irregular, non-ellipsoidal shapes. Additionally, the orientation of the cluster was only tested in either a parallel to flow or perpendicular to flow condition, so varying angle of attack with ellipsoidal clusters could provide useful data to further characterize the behavior of more realistic fragmentation events. Finally, the number of spheres and compositions were held the same throughout these experiments. Future work should seek to repeat similar experiments with different

cluster populations, uneven fragment sizes, or with the inclusion of dust or powder to better characterize real-world meteoroid fragmentation scenarios.

References

[1] Chapman, C.R., "Meteoroids, Meteors, and the Near-Earth Object Impact Hazard," *Earth Moon Planet*, Vol. 102, 2008, pp. 417–424.
doi: 10.1007/s11038-007-9219-6

[2] Bland, P., and Artemieva, N., "Efficient disruption of small asteroids by Earth's atmosphere," *Nature*, Vol. 424, No. 6946, 2003, pp. 288–291.
doi: 10.1038/nature01757

[3] Whalen, T.J., and Laurence, S.J., "Experiments on the separation of sphere clusters in hypersonic flow," *Exp Fluids*, Vol. 62, No. 70, 2021.
doi: 10.1007/s00348-021-03157-z

[4] Zhu, W., and Laurence, S.J., "An Experimental Investigation on Various Types of Sphere Clusters Separating in Hypersonic Flow," AIAA 2024-3968. *AIAA AVIATION Forum and ASCEND* 2024. July 2024.
doi: 10.2514/6.2024-3968

[5] Whalen, T.J., "Aerodynamic Separation of Fragmented Bodies in High-Speed Flow," PhD dissertation, 2021.

[6] Laurence, S.J., Deiterding, R., and Hornung, G., "Proximal bodies in hypersonic flow," *Journal of Fluid Mechanics*, Vol. 590, 2007, pp. 209–237.
doi: 10.1017/S0022112007007987

[7] Marwege, A., Willems S., Gülhan A., Aftosmis, M.J., and Stern, E.C., "Superposition Method for Force Estimations on Bodies in Supersonic and Hypersonic Flows," *Journal of Spacecraft and Rockets*, Vol. 55, No. 5, 2018, pp. 1–15.
doi: 10.2514/1.A34128

[8] Seltner, P., Willems, S., Gülhan, A., Stern, E.C., Brock, J., and Aftosmis, M.J., "Aerodynamics of inclined cylindrical bodies free-flying in a hypersonic flowfield," *Exp Fluids*, Vol. 62, No. 9, 2021, pp. 182.
doi: 10.1007/s00348-021-03269-6.

[9] Duchene, T.A., and Laurence, S.J., "The aerodynamics of sharp- and filet-edged cylinders in high supersonic flow," *Exp Fluids*, Vol. 66, No. 33, 2025.
doi: 10.1007/s00348-025-03968-4

[10] Laurence, S.J., and Deiterding, R., "Shock-wave surfing," *Journal of Fluid Mechanics*, Vol. 676, 2011, pp. 396–431.
doi: 10.1017/jfm.2011.57

[11] Anderson, J. D., *Hypersonic and High-Temperature Gas Dynamics*, 2nd ed., AIAA Education Series, 2006.

[12] Laurence, S.J., "On tracking the motion of rigid bodies through edge detection and least-squares fitting," *Exp Fluids*, Vol. 52, 2012, pp. 387–401.
doi: 10.1007/s00348-011-1228-6

[13] De Silva, R.S., Whalen, T.J., and Laurence, S.J., "Free-Flight Optical Tracking using Artificial Image Generation," AIAA 2023-3712. *AIAA AVIATION 2023 Forum*. June 2023.
doi: 10.2514/6.2023-3712